ORNL/TM-2017/187

Transportable, Low-Dose Active Fast-Neutron Imaging

Seth McConchie
Daniel Archer
John Mihalczo
Blake Palles
Michael Wright

July 2017

OAK RIDGE NATIONAL LABORATORY
MANAGED BY UT-BATTELLE FOR THE US DEPARTMENT OF ENERGY

ORNL/TM-2017/187

Nuclear Security and Isotope Technology Division

TRANSPORTABLE, LOW-DOSE ACTIVE FAST-NEUTRON IMAGING

Seth McConchie
Daniel Archer
John Mihalczo
Blake Palles
Michael Wright

Date Published: July 2017

Prepared by
OAK RIDGE NATIONAL LABORATORY
Oak Ridge, TN 37831-6283
managed by
UT-BATTELLE, LLC
for the
US DEPARTMENT OF ENERGY
under contract DE-AC05-00OR22725

CONTENTS

LIST OF FIGURES v
LIST OF TABLES v
ACRONYMS vii
ABSTRACT 1
1. TECHNIQUE AND INSTRUMENTATION 1
2. IMAGE RECONSTRUCTION 4
3. IMAGE ANALYSIS 7
4. MEASUREMENT EXAMPLE 13
5. CONCLUSION 14
REFERENCE DOCUMENTS 15

LIST OF FIGURES

Figure 1. Diagram showing the spatial resolution dependence upon the line of response between the detector and neutron production spot. 2
Figure 2. Diagram of the instrumentation for the Nuclear Materials Identification System (NMIS) active fast-neutron imager. 3
Figure 3. Diagram of the instrumentation for the Advanced Portable Neutron Imaging System (APNIS). 4
Figure 4. Example ray-trace demonstrating coordinate system nomenclature. 5
Figure 5. Fundamental steps of the data processing from the signal collection to the reconstruction. 6
Figure 6. Example comparison of the FBP and MLEM reconstructions of INL Inspection Object 9. 6
Figure 7. Uranium metal annuli with (a) no gap, (b) a 5-mm gap, (c) a 1-mm gap, and (d) a 0.5-mm gap. 8
Figure 8. Comparison of the ray-trace before and after the application of the point-spread function (PSF) for the annulus with no gap. 9
Figure 9. Comparison of the measurement predictions for the annuli from Figure 7. 10
Figure 10. Uranium metal annuli with (a) no gap, (b) a 5-mm gap, (c) a 1-mm gap, and (d) a 0.5-mm gap, shielded by 127 mm of polyethylene. 10
Figure 11. Comparison of the measurement predictions for the polyethylene-shielded annuli from Figure 10. 11
Figure 12. Measurement time as a function of gap thickness for the bare annulus and polyethylene-shielded annulus using CL=0.99 and void rate 200 cps. 13
Figure 13. Filtered back projection reconstruction of two uranium metal annuli. The nominal gap of 3 mm between the annuli is detectable using 1-inch imaging detectors and a 5-mm neutron production spot size. 14

LIST OF TABLES

Table 1. Materials and their attenuation at 14 MeV. 8
Table 2. Parameters of the ray-tracing example 9

ACRONYMS

API	Associated Particle Imaging
APNIS	Advanced Portable Neutron Imaging System
ASIC	Application-Specific Integrated Circuit
CDF	Cumulative Distribution Function
cCDF	Complementary Cumulative Distribution Function
Ce	Cerium (element)
cm	Centimeter
cps	Counts per Second
D-D	Deuterium-Deuterium
D-T	Deuterium-Tritium
FBP	Filtered-Back Projection
FNMIS	Fieldable Nuclear Materials Identification System
INL	Idaho National Laboratory
MeV	Megaelectronvolt (million electron volts or 10^6 volts)
MFP	Mean Free Paths
MLEM	Maximum Likelihood Expectation Maximization
mm	Millimeter
NIM	Nuclear Instrumentation Module
NMIS	Nuclear Materials Identification System
ORNL	Oak Ridge National Laboratory
PCI	Peripheral Component Interconnect
PET	Positron-Emission Tomography (scanner)
PMMA	Polymethylmethacrylate (acrylic)
PMT	Photomultiplier Tube
PSF	Point-Spread Function
PVT	Polyvinyl Toluene
VNIIA ING-27	Russian API deuterium-tritium neutron generator
YAP	Yttrium Aluminum Perovskite

ABSTRACT

This document contains a description of the method of transportable, low-dose active fast-neutron imaging as developed by ORNL. The discussion begins with the technique and instrumentation and continues with the image reconstruction and analysis. The analysis discussion includes an example of how a gap smaller than the neutron production spot size and detector size can be detected and characterized depending upon the measurement time.

1. TECHNIQUE AND INSTRUMENTATION

This technique was developed for applications that require imaging of radiographically thick items with high-Z materials and transportability to enable the imager to be taken to the item. The transportability capability necessitates the incorporation of portable neutron sources that can be considered low dose in most cases compared to fixed-installation accelerators employed in neutron imaging facilities. Transportable neutron imaging can be accomplished at some level with any portable neutron source, but fast-neutron sources tend to be most useful for arbitrary item imaging because of their emitted neutron penetrability. Typical portable fast-neutron sources have little to no directional emission bias such that at least half of the source neutrons are not used for transmission imaging and add to the detector background via scattering in the surrounding environment. Time-tagging the source neutrons and counting only those neutrons having the expected time-of-arrival in the detector reduces the background originating from the environment and any radioactive emitters near the detectors. The other primary contribution to the detector background originates from scattering in the item. As the item thickness in mean free paths (mfp) increases, all paths through the item become equally likely to contribute to the observed transmission signal. Direction-tagging the source neutrons reduces the background originating from scattering in the item. In effect, both types of tagging seek to minimize the background as much as possible to maximize the contrast resolution.

The only known commercially available neutron source that provides both time and direction information for each source neutron is an associated particle imaging (API) neutron generator. API neutron generators can be fabricated to employ the deuterium-deuterium (D-D) or deuterium-tritium (D-T) fusion reactions. API D-T neutron generators are more widely used because of the penetrative capability of 14 MeV neutrons as compared to 2.5 MeV neutrons and the neutron output advantage for the same beam current because of the two-orders-of-magnitude difference in the cross sections. Additionally, the API D-T neutron generator approximates a point source, enabling geometric magnification as a function of item width and distance from the source. Halving the distance of the source-to-item distance translates into an item shadow that is twice as large. The spatial resolution is driven by the solid angle subtended by each detector and the neutron production spot, as shown in Figure 1. As the item is placed closer to the spot, the spatial resolution improves but is ultimately limited by the spot size.

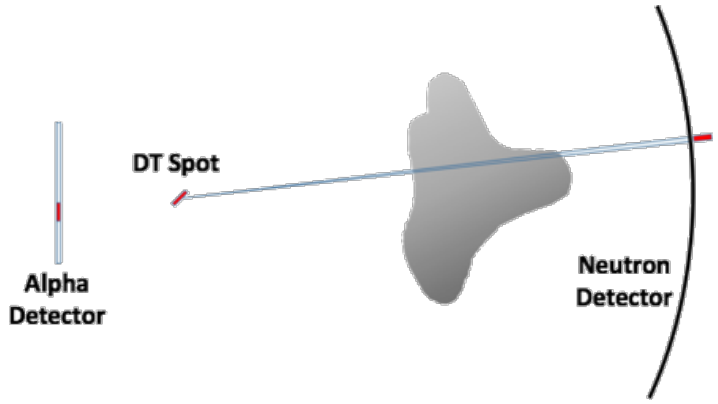

Figure 1. Diagram showing the spatial resolution dependence upon the line of response between the detector and neutron production spot.

The first ORNL active fast-neutron imagers leveraged the Nuclear Materials Identification System (NMIS) time coincidence platform [1]. This platform is characterized by a high-speed low-channel-density data acquisition processor embedded on custom peripheral component interconnect (PCI) boards that receives timing gates with nanosecond precision from constant fraction discriminators. Histograms representing the time between events are constructed from the event data stream to enable an analysis of specific timing signatures. The latest NMIS implementation uses either a Thermo-Fisher Scientific API-120 or VNIIA ING-27 DT neutron generator. The API-120 has a 5-mm target spot and contains an embedded Schott 75C fiber optic faceplate with a YAP(Ce) crystal. A Hamamatsu H9500 photomultiplier tube (PMT) is optically coupled to the faceplate viewport, and one horizontal row of 16 pixels is instrumented. The angular resolution of each emitted neutron is approximately 5°, and the opening angle is approximately 50°. The neutron generator operates typically at 4×10^7 n/s/4π maximum output. The ING-27 has a 3-mm target spot and contains an embedded Si detector with 15 pixels. The angular resolution of each emitted neutron is approximately 4°, and the opening angle is approximately 60°.

The detector array of 32 Scionix EJ-200 1×1×4-in. plastic scintillators in NMIS detects the transmitted 14-MeV neutrons. These detectors are typically located between 110 cm and 115 cm from the neutron generator in the same horizontal plane. For an API-120 neutron output of 4×10^7 n/s/4π, an average alpha count rate is 8×10^3 alphas/s per alpha pixel; the average detector count rate is 7×10^2 events/s per detector; and the average alpha-source neutron coincidence rate is 2×10^2 events/s. The timing resolution for the entire imager is approximately 1 ns. The neutron generator and detectors are affixed to a frame that can be moved vertically to permit images to be collected at several heights. The detectors are typically moved horizontally some fraction of a detector width to subsample the detector space and artificially provide more image pixels so that edge features can be better sampled. Most images have been collected with four subsamples so that projections are displayed on 128 pixels instead of 32 pixels. A turntable is available to rotate the object for multiple projections, enabling full computed tomography. A laboratory version of NMIS uses Nuclear Instrumentation Model (NIM) electronics for the pulse processing and supplying high voltage to the detectors. A fieldable version of NMIS (FNMIS) replaced the NIM electronics with application-specific integrated circuit (ASIC) boards. Both imagers optionally include an array of EJ-200 12×12×4-in. plastic scintillators for the detection of induced fission neutrons [2]. A diagram of the NMIS instrumentation is given in Figure 2.

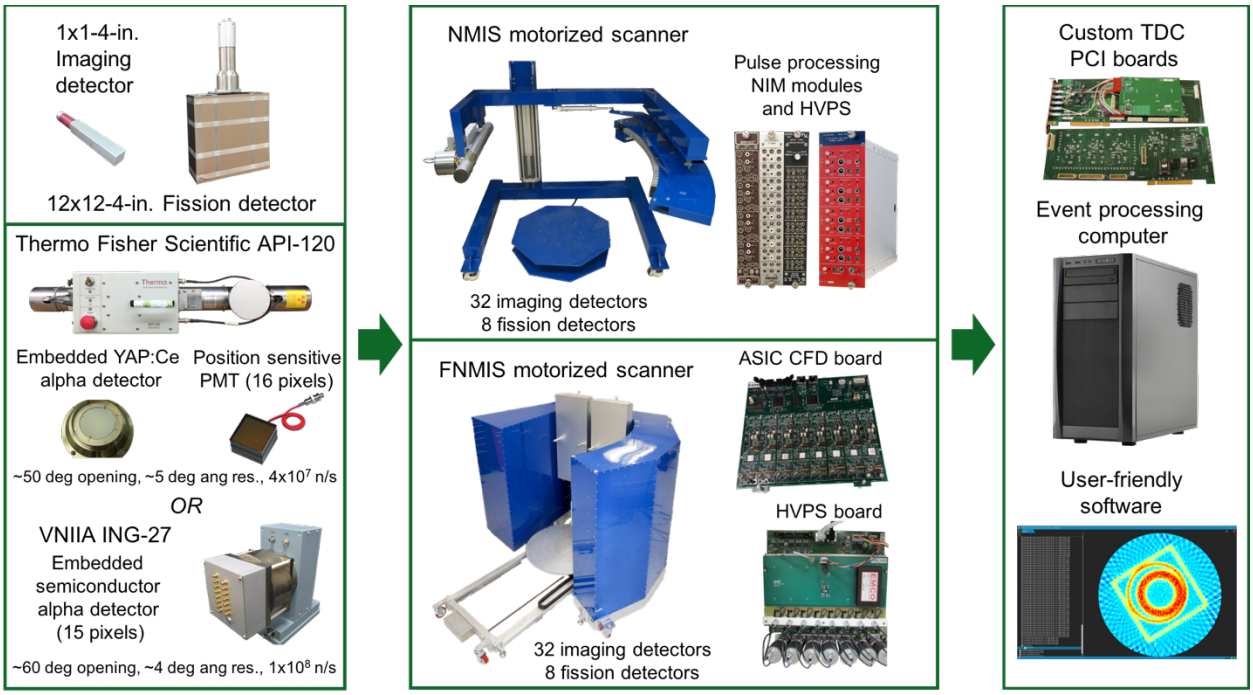

Figure 2. Diagram of the instrumentation for the Nuclear Materials Identification System (NMIS) active fast-neutron imager.

A vertical scan of the item can require several hours with NMIS depending upon the desired quality of the image. Scaling up the area of the NMIS detector array is nontrivial because of the instrumentation and data acquisition challenge with the 1×1×4-in. detectors. Using the pixelated block detector concept developed by the Positron-Emission Tomography (PET) imaging community, transmission block detectors were developed using the EJ-200 plastic scintillator [3]. Block detectors have been fabricated with the pulse shape discrimination (PSD) plastic EJ-299-33 but have not been used for this type of imaging. Each block detector has dimensions of 10.8×10.8×32.3 cm with an active volume of 10.39×10.39×5 cm. The EJ-200 volume has internal 3M Vikuiti reflector planes to optically segment the block into 100 1-cm pixels per detector. The polyvinyl toluene (PVT) pixel block is backed by an acrylic polymethylmethacrylate (PMMA) light guide with dimensions 10.39×10.39×2.8 cm and is viewed by four Hamamatsu R9779 PMTs. To date, the block detectors have been read out with a Siemens Preclinical Inveon PET data acquisition module where the pixel of the neutron or gamma event is determined with Anger logic. The data acquisition module can also perform coincidence matching, but all single events are saved to disk typically so that coincidence matching can be performed offline. A detector array of block detectors scales upward in area more easily. An array of these detectors has been deployed in arrangements of 4×8, 2×16, and 3×11 to realize 3200 to 3300 1-cm pixels. These deployments have used the same API-120 model that has been used for NMIS and are known as variations of the Advanced Portable Neutron Imaging System (APNIS). The H9500 interfaces with the faceplate viewport with a custom light guide and is instrumented to realize 512 pixels from two 4-corner readouts with a resistive network board [4]. A diagram of the APNIS instrumentation is given in Figure 3. In summary, the APNIS concept enables improved spatial resolution over NMIS, the ability to obtain 2-D images without vertical scanning, and multiple detection modes on common hardware.

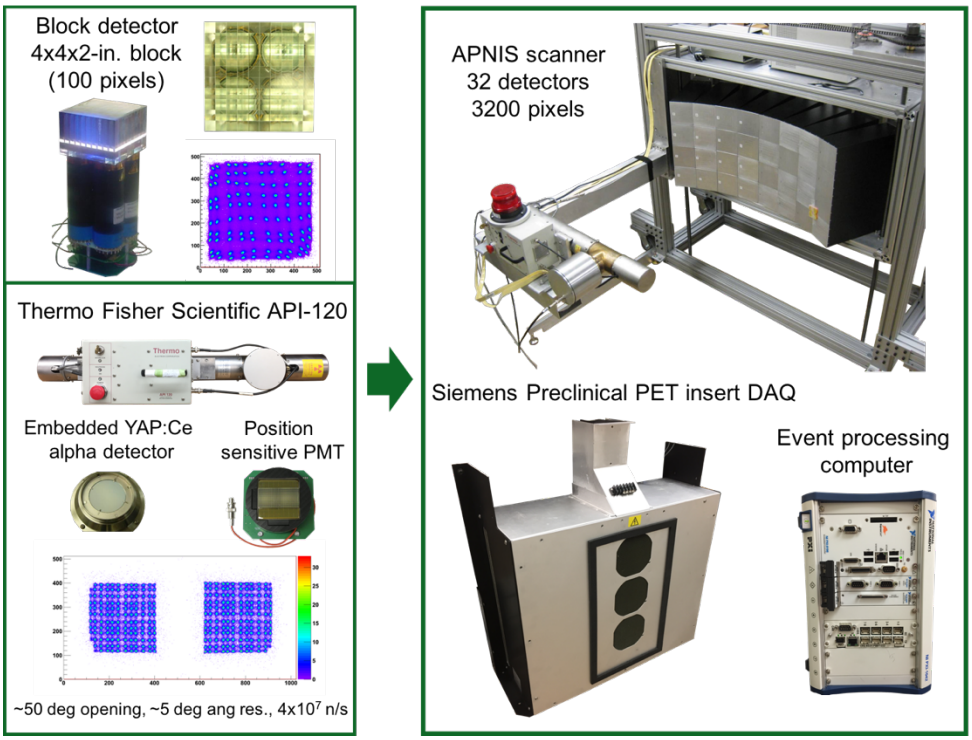

Figure 3. Diagram of the instrumentation for the Advanced Portable Neutron Imaging System (APNIS).

2. IMAGE RECONSTRUCTION

The image reconstruction seeks to reconstruct the map of neutron attenuation coefficients from the observed transmitted counts in the detector. Letting I_0 be the number of source neutrons emitted along each path from the source to the detector and $\mu(x,y)$ be the neutron attenuation coefficient map in two dimensions, the number of neutrons, I, transmitted to the detector along path $\vec{s}$ is

$$I = I_0 \exp\left(-\int \mu(x,y)ds'\right)\Big|_{\text{path } \vec{s}} . \quad (1)$$

The item geometry is described with the $x-y$ coordinate system. As the source and detector can have an arbitrary location and orientation with respect to the item, the observed transmitted counts are described in the $t-\theta$ coordinate system, where θ is the angle of rotation describing the relative orientation. The coordinate transformation is

$$t = x\cos\theta + y\sin\theta . \quad (2)$$

Using Eq. (1) and the coordinate system definitions, the projection $\boldsymbol{P}_\theta(t)$ is defined as

$$\boldsymbol{P}_\theta(t) \stackrel{\text{def}}{=} -\ln\left(\frac{I(t)}{I_0(t)}\right)\Big|_\theta = \int_{\text{path } t} \mu(x,y)ds' , \quad (3)$$

representing the total attenuation along each path through the item from the source to the detector. An example ray-trace demonstrating the coordinate systems and path integral result is shown in Figure 4.

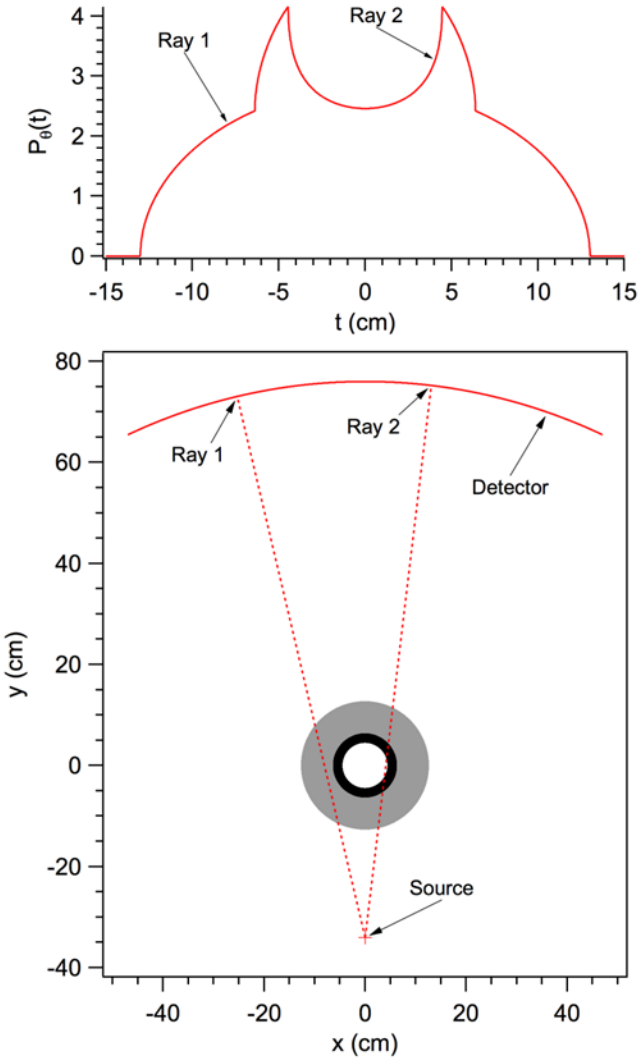

Figure 4. Example ray-trace demonstrating coordinate system nomenclature.

The fundamental steps of the data processing are shown in Figure 5. The anode pulses from the detector array and the alpha detector are processed to determine the originating pixel and the time-of-arrival. The time-of-arrivals are sorted to construct a time-of-flight spectrum to determine the number of transmitted 14-MeV neutrons. The attenuation profile, or projection, is calculated per Eq. (3) for each rotation of the item and corrected to remove the item in-scatter contribution. The sinogram is constructed with the projections and input to the image reconstruction algorithm. ORNL uses two image reconstruction algorithms: filtered back-projection (FBP) or maximum likelihood expectation maximization (MLEM). The filtered back-projection implementation follows the equiangular fan-beam projection algorithm described in Reference [5]. The coordinate system from Eq. (2) is also from Reference [5] and will be used later in this document. The MLEM implementation is based upon the algorithm developed in Reference [6]. FBP images are typically constructed immediately after measurement completion and require 10 or fewer seconds of computation time. While using a large number of projections tends to minimize the number of artefacts, projections through highly attenuating items can have low statistics due to the limited source intensity, requiring a balance between the statistical convergence of each projection and the number of projections for a fixed measurement time. From experience, the number of projections

is usually limited to between 30 and 60 for items without radial symmetry. The low number of projections leads to streaking artefacts, which can interfere with the image interpretation. As MLEM reconstructions are free from the streaking artefacts, they are also performed but require several minutes to complete. Recent advancements have realized MLEM reconstructions in less than a second of computer time. An example comparison of FBP and MLEM reconstructions of Idaho National Laboratory (INL) Inspection Object 9 [7] using a version of NMIS is shown in Figure 6. ORNL currently has an NA-22 project to develop and implement algorithms to perform 3-D tomography.

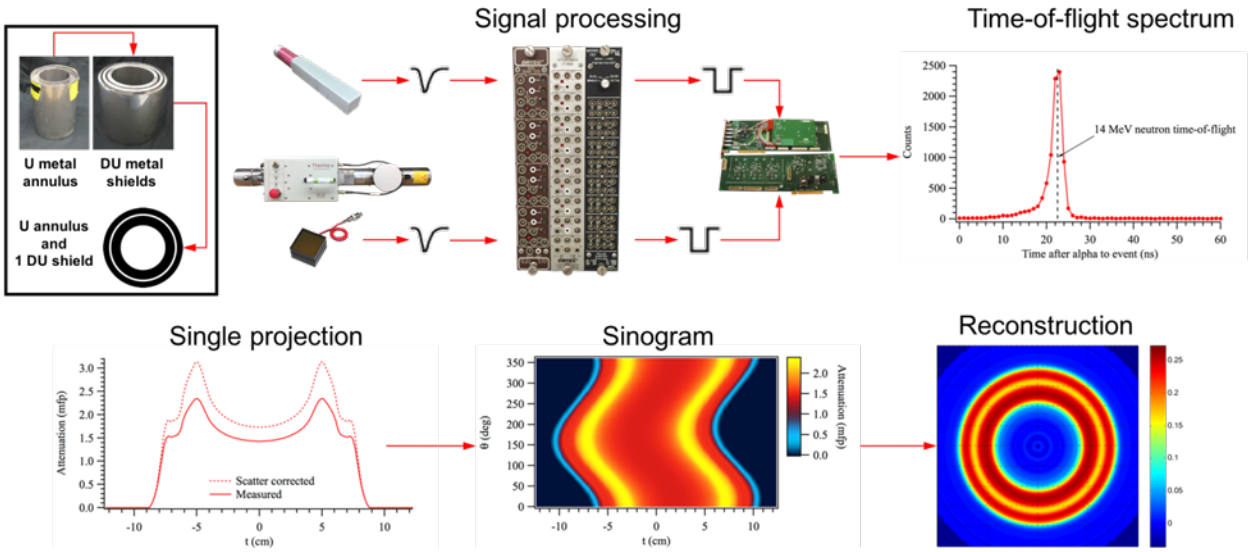

Figure 5. Fundamental steps of the data processing from the signal collection to the reconstruction.

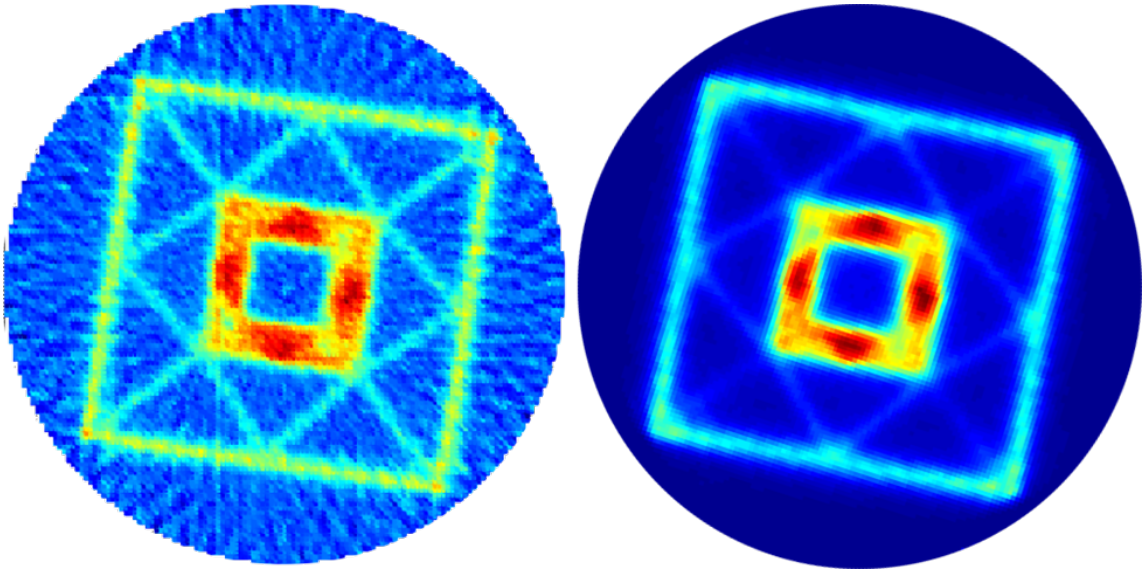

Figure 6. Example comparison of the FBP and MLEM reconstructions of INL Inspection Object 9.

The current in-scatter correction for an NMIS imaging measurement involves subtracting the level of excess counts in the extreme tails of the alpha detector-transmission detector profile response when an item is absent. This level is determined by the pixel locations at which the response deviates from

Gaussian behavior, which tends to be approximately 4% of the peak. These counts are assumed to not be directly transmitted neutrons but rather scattered neutrons, originating in part from inter-detector scatter. When the item is present, the same subtraction is performed in the alpha-detector response and empirically has been a good approximation for the forward scatter contribution for most items. Details of the scatter subtraction algorithm can be found in Reference [8].

3. IMAGE ANALYSIS

An analysis of a reconstructed image typically has three goals:

1. identify the materials and their location,

2. perform a dimensional analysis of simple shapes (e.g., rectangles and circles, *and*

3. locate any anomalous features within the reconstruction that are unexpected (if the item geometry is expected) and can conform to complex shapes.

If the in-scatter correction is accurately performed such that the observed attenuation map reflects the actual attenuation map, then the materials shown in Table 1 can be identified by their characteristic neutron attenuation coefficients within the reconstruction. The dimensional analysis is performed with a ray-trace fitting algorithm that populates the image space with shapes from a list of simple shapes (e.g., rectangles, circles, etc.) and varies the dimensions and neutron attenuation coefficients until the best fit of the measured projections and calculated projections is accomplished. The algorithm accounts for the neutron production spot size and detector response, including the size of the detector and its location relative to the center of the item and the neutron production spot. The user has the option of letting the algorithm guess all input parameters from the reconstructed image, namely, the numbers and types of shapes, their dimensions, and neutron attenuation coefficients. However, typical use consists of identifying the number of shapes in the reconstructed image and letting the algorithm guess the dimensions and neutron attenuation coefficients. This level of user intervention prevents the algorithm from identifying image artefacts as shapes. An artefact arises when the statistical uncertainty of the measured attenuation along some path is larger than the gradient of the actual attenuation. Divergence of the fit or the detection of a local minimum is possible, especially with poor input guesses. While the accuracy of the dimensional analysis is improved with a priori knowledge of the item geometry, such knowledge is not required. The reconstructed image reveals the internal geometry, provides initial guesses to the fitting algorithm, and can be used to qualitatively check the fit results.

Anomalous features are unexpected features, possibly composed of complex shapes, that can require significant human interpretation to accurately characterize them. Features smaller than the neutron production spot size and the detector size can be detected and, to a limited extent, characterized. In the context of this document, a feature is successfully “detected” if it can be distinguished from the surrounding material in the image. A feature is successfully “characterized” if its size can be accurately measured. For a fixed spot size and detector size, the detection and characterization limits depend upon the measurement time to minimize the statistical error and the scale of the systematic error associated with the fit. In this context, negligible statistical errors correspond to long measurement times, large neutron source fluxes, or both. Negligible systematic errors correspond to excellent knowledge of the neutron production angular and timing distributions and a high-fidelity 3-D image analysis, including an accurate in-scatter subtraction.

Table 1. Materials and their attenuation at 14 MeV. The list is partitioned into low-Z and high-Z materials, and example exceptions are noted

Material		Attenuation @14 MeV (cm^{-1})
Low-Z materials*		0.10 to 0.14
	Aluminum	0.105
	Polyethylene	0.11
	Graphite	0.112
	Explosives	0.13 to 0.14
High-Z materials‡		0.17 to 0.32
	Lead	0.176
	Steel	0.22
	Uranium metal	0.28
	Tungsten	0.33

*Example low-Z material exception: Titanium (0.13 cm^{-1})
‡Example high-Z material exception: Beryllium (0.19 cm^{-1})

The following example demonstrates the statistical limits with a uranium metal annulus having a 3.50-in. (8.89-cm) inner diameter, 5.00-in. (12.70-cm) outer diameter, and 6.00-in. (15.24-cm) height. The annulus without the gap and the annuli with a 5-mm, 1-mm, and 0.5-mm gap are shown in Figure 7. A two-dimensional ray-tracer was used to predict the measurement result of each annulus with and without the gap. The ray-tracer forward-projected a set of rays from the neutron source through the annulus, located 34 cm from the source and represented with high fidelity by pixels, to the detector array located 110 cm from the source. Then the ray-tracer applied a point-spread function that approximates the effect of the neutron production spot size and detector size for an NMIS imager using a 5-mm neutron production spot size and 2.5×2.5×10-cm detectors. The parameters of the ray-tracing example are given in Table 2. A comparison of the ray-trace before and after the application of the point-spread function is shown in Figure 8. For the annuli from Figure 7, a comparison of the measurement predictions is shown in Figure 9. Without consideration for the statistical error, the annuli are distinguishable despite the gaps being smaller than the neutron production spot size and detector size. The ability to distinguish the annuli becomes more challenging when they are shielded, such as with several inches of a low-Z material. The ray-trace was repeated on the same annuli shielded by 5 in. (127 mm) of polyethylene, as shown in Figure 10. The measurement predictions are shown in Figure 11. As with the unshielded annuli, the polyethylene-shielded annuli are distinguishable without consideration of the statistical error.

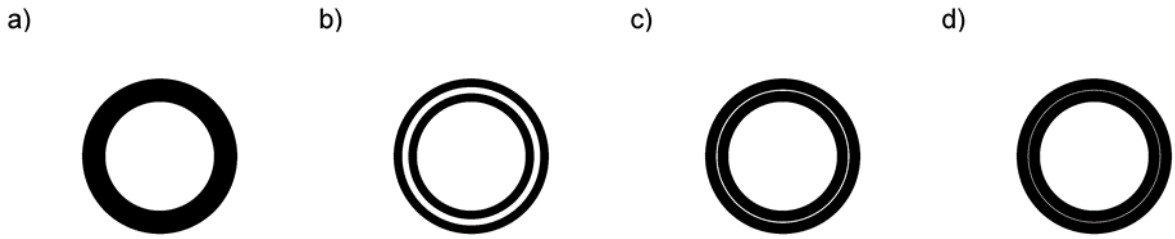

Figure 7. Uranium metal annuli with (a) no gap, (b) a 5-mm gap, (c) a 1-mm gap, and (d) a 0.5-mm gap.

Table 2. Parameters of the ray-tracing example

Parameter	Value
Source-to-detector distance	110 cm
Source-to-center (of item) distance	34 cm
Opening angle of detector array	50.6°
Pixel dimensions for annulus representation	25.6×25.6 microns
Number of rays	2048
Number of detectors	32
Number of subsamples	4
Projection pixels	128

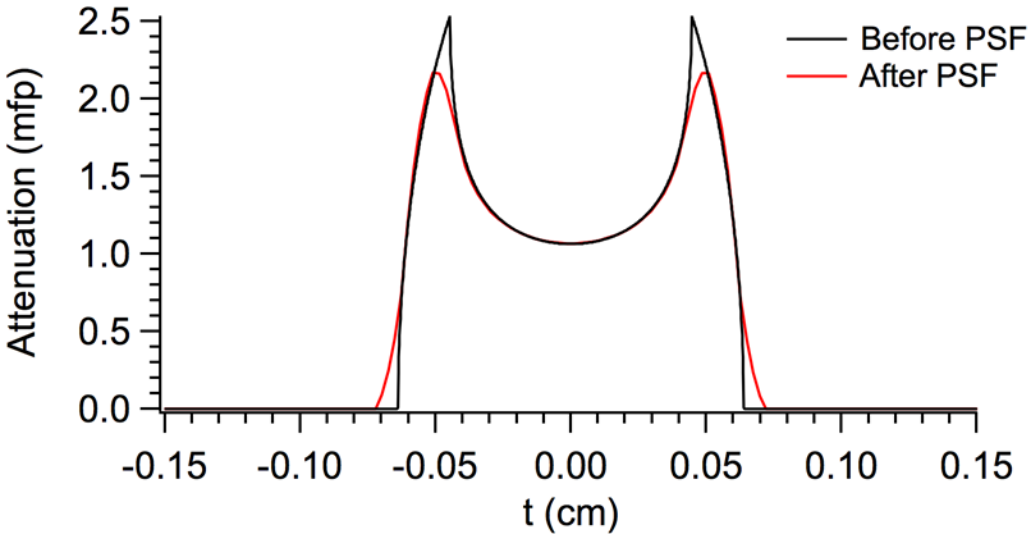

Figure 8. Comparison of the ray-trace before and after the application of the point-spread function (PSF) for the annulus with no gap.

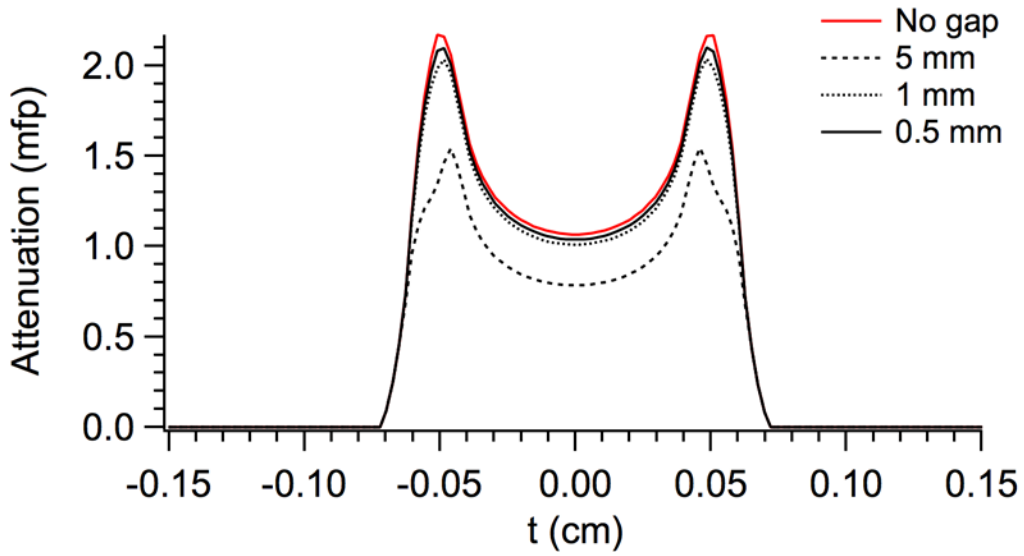

Figure 9. Comparison of the measurement predictions for the annuli from Figure 7. Without consideration for the statistical error, the annuli are distinguishable.

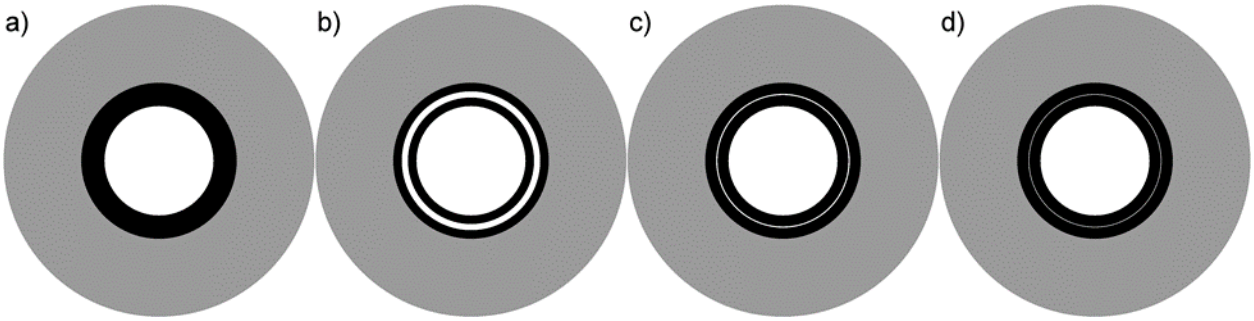

Figure 10. Uranium metal annuli with (a) no gap, (b) a 5-mm gap, (c) a 1-mm gap, and (d) a 0.5-mm gap, shielded by 127 mm of polyethylene.

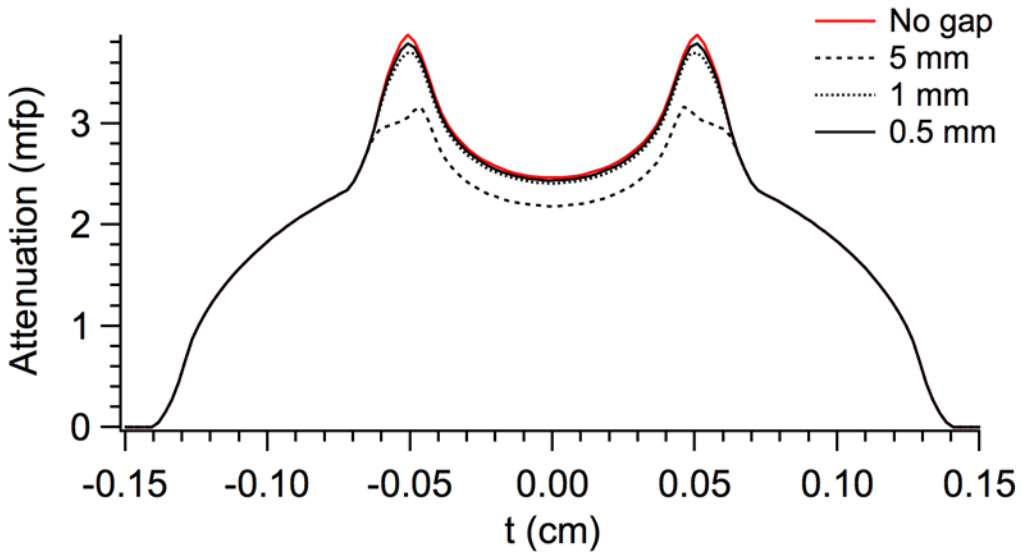

Figure 11. Comparison of the measurement predictions for the polyethylene-shielded annuli from Figure 10. Without consideration for the statistical error, the annuli are distinguishable.

The measurement time required to detect a gap as a function of its size depends upon the ability to distinguish between, or contrast, the observed attenuations when the gap is present or absent. One method for estimating the measurement time to contrast two paths with different attenuations uses the probability density distribution for the attenuation. In this context, the attenuation a is defined as

$$a \stackrel{\text{def}}{=} -\ln\left(\frac{S}{S_0}\right) = -\ln\left(\frac{T-B}{S_0}\right), \tag{4}$$

where S is the transmitted (i.e., unscattered), detected 14-MeV neutrons; B is the background counts including the in-scattered neutrons and other neutrons or gammas arriving in the time window uncorrelated to the alpha event; and S_0 is the void counts. In a measurement, T represents the total counts observed including the transmitted counts and background counts.

If T and B are Gaussian distributed, a probability transformation of the distributions for T and B using Eq. (4) yields the probability distribution of attenuations along path k as

$$P_k(a) = \frac{1}{\sqrt{2\pi}\sigma_k}\frac{2}{\left(1+\operatorname{erf}\left(\frac{\lambda_k}{\sqrt{2}\sigma_k}\right)\right)}\exp\left(-\frac{(\exp(-a)-\lambda_k)^2}{2\sigma_k^2}-a\right), \tag{5}$$

where

$$\lambda_k = e^{-\langle a_k\rangle}\,\sigma_k^2 = \frac{\dot{S}_0 e^{-\langle a_k\rangle} + 2\langle \dot{B}_k\rangle}{\dot{S}_0^2}\frac{1}{t} = \frac{\dot{\sigma}_k^2}{t}\,, \tag{6}$$

and erf (x) is the usual "error function." In this framework, $\langle x\rangle$ is the expectation value of x and $\dot{x} = x/t$ with t being the measurement time. For two paths $k = 1$ and $k = 2$, the probability distributions should have as little overlap in a as possible. One metric for measuring the overlap uses the cumulative

distribution function (CDF) of Eq. (5) for the path with lesser attenuation and the complementary CDF ($cCDF$) for the path with the greater attenuation. The CDF for path k is

$$CDF_k(a) = \frac{1}{\left(1 + \text{erf}\left(\frac{\lambda_k}{\sqrt{2}\sigma_k}\right)\right)}\left(1 - \text{erf}\left(\frac{e^{-a} - \lambda_k}{\sqrt{2}\sigma_k}\right)\right) = 1 - cCDF_k(a). \quad (7)$$

Assuming $a_1 > a_2$, there exists some value $a = a_t$ for which the $cCDF_{k=1}$ and $CDF_{k=2}$ are equal. Defining the confidence level CL to be

$$CL \stackrel{\text{def}}{\equiv} cCDF_{k=1}(a_t) = CDF_{k=2}(a_t), \quad (8)$$

Eq. (8) may be interpreted as the probability that paths 1 and 2 are correctly distinguished. The special value $a = a_t$ yields a transcendental equation in t, CL, λ_k, and $\dot{\sigma}_k$. Measurement times will typically range from seconds to hours for typical geometries, enabling the approximation

$$\text{erf}\left(\frac{e^{-\langle a_k \rangle}\sqrt{t}}{\sqrt{2}\dot{\sigma}_k}\right) \sim 1. \quad (9)$$

This approximation simplifies the transcendental equation such that the measurement time can be solved algebraically to give

$$t = \frac{2}{\left(\exp(-\langle a_1 \rangle) - \exp(-\langle a_2 \rangle)\right)^2}(\dot{\sigma}_2 + \dot{\sigma}_1)^2\left(\text{erfc}^{-1}(2CL)\right)^2. \quad (10)$$

Eq. (10) was used to estimate the minimum measurement time to detect the gap as a function of its size. The background term in Eq. (6) was assumed to be dominated by the in-scattering in the item and was conservatively estimated to include all elastic scatters events in the item. There are two reasons for this conservative estimate. First, the conservative estimate gives an upper bound for the measurement time and tends to be increasingly accurate as the item attenuation increases. Second, a simple formula can be written for the total background rate due to all elastic scatters:

$$\langle \dot{B} \rangle \approx \dot{S}_0\left(e^{\langle \mu_e x \rangle} - 1\right)e^{-\langle \mu x \rangle}, \quad (11)$$

where μ is the total attenuation coefficient and μ_e is the attenuation coefficient due to elastic scattering. For most nuclei, the elastic scatter cross section is approximately half the total cross section, and the Eq. (11) becomes

$$\langle \dot{B} \rangle \approx \dot{S}_0\left(e^{\langle \mu x \rangle/2} - 1\right)e^{-\langle \mu x \rangle} = \dot{S}_0\left(e^{\langle a \rangle/2} - 1\right)e^{-\langle a \rangle}. \quad (12)$$

The background can be estimated more accurately by considering that only some fraction of the source neutrons undergoing a single elastic scatter will forward scatter in the direction of the detector. The next order corrections consider those neutrons that undergo two, three, or more elastic scatters and forward scatter in the direction of the detector. The mathematical form of the background based upon these possibilities is a function of the materials, source, and detectors and is much more challenging to evaluate than Eq. (12). Arguably, a radiation transport simulation is a better approach to estimate the background with high accuracy.

For $CL = 0.99$ and $\dot{S}_0 = 200$ cps, the measurement time as a function of gap thickness through the annulus center is shown for the bare annulus and the polyethylene-shielded annulus in Figure 12. A 1-mm gap requires 227 seconds in the bare case and 2250 seconds in the polyethylene-shielded case. These measurement times become 929 seconds and 9310 seconds, respectively, for a 0.5-mm gap.

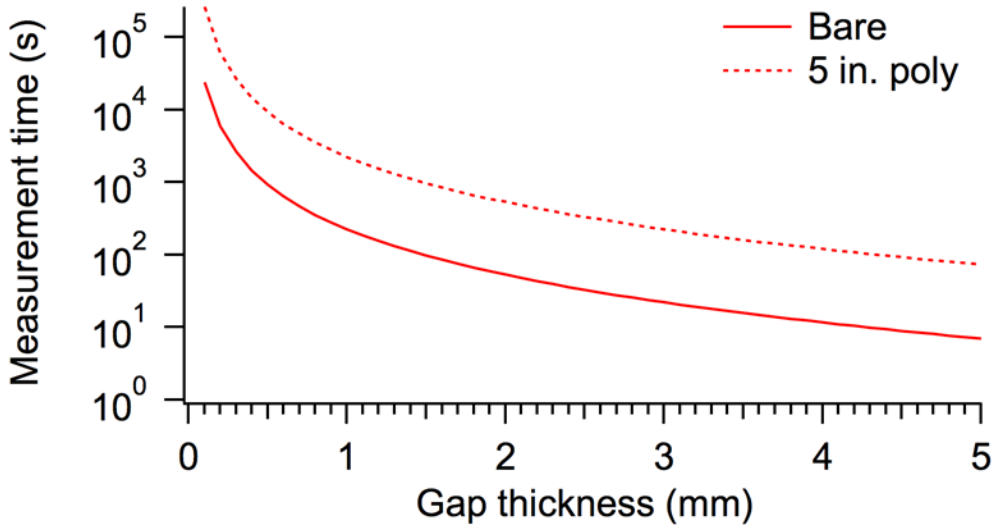

Figure 12. Measurement time as a function of gap thickness for the bare annulus and polyethylene-shielded annulus using CL=0.99 and void rate 200 cps.

4. MEASUREMENT EXAMPLE

An example measurement demonstrating the ability to detect a feature smaller than the neutron production spot size and the detector size is shown in Figure 5. The geometry is a uranium metal annulus surrounded by another uranium metal annulus where both annuli are canned with 0.6-mm thick stainless steel to prevent alpha contamination. The inside annulus has a 3.5-in. (8.9-cm) inner diameter, 5.0-in. (13-cm) outer diameter, and 6.0-in. (15-cm) height. The outside annulus has a 5.3-in. (8.9-cm) inner diameter, 6.2-in. (16-cm) outer diameter, and 6.0-in. (15-cm) height. The nominal gap between the inside and outside annuli is approximately 3 mm. A research and development version of NMIS similar to the system described in Section 1 was used to image the geometry, and a detailed description of the measurement can be found in Reference [9]. The tomographic reconstruction shown in Figure 5 is shown again in Figure 13. The reconstruction represents 30 minutes of data at a single view. As the geometry is rotationally symmetric, the statistically converged data for a single view was used to simulate a large number views. While the nominal 3-mm gap is detectable using 1-inch imaging detectors and a 5-mm neutron production spot size, the effect of the detector size and spot size is evident in the observed attenuation coefficient associated with the gap. Instead of an attenuation coefficient of zero, the measured value is ~0.15 cm^{-1}, consistent with, for example, a dense low Z material. As the 3-mm gap is known to be present, a correction to the reconstruction to accurately identify the edges may be possible. However, ORNL traditionally analyzes the projections, not the reconstruction, with a ray-tracing algorithm incorporating the appropriate point spread function. The ray-trace fit solution with the correct attenuation coefficient for the gap would yield the observed projection.

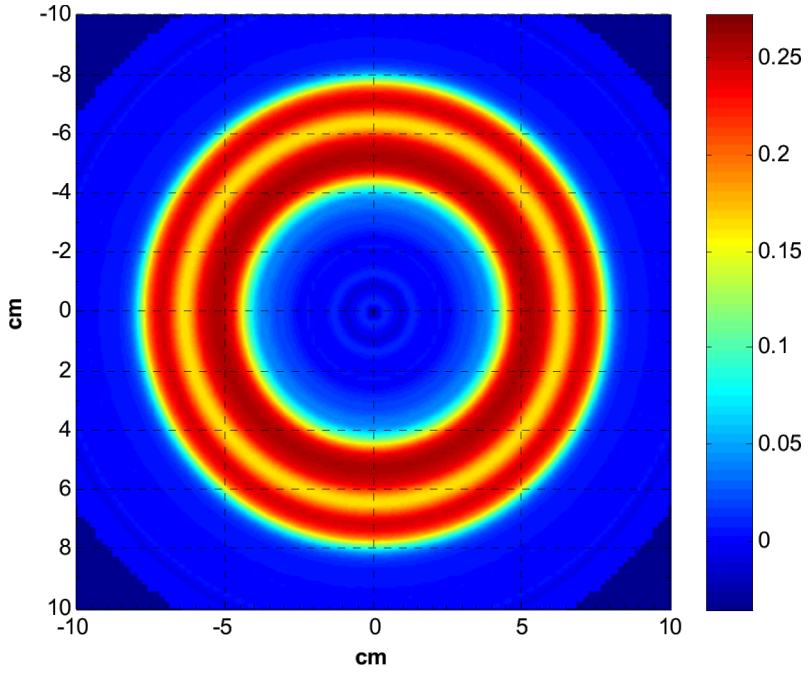

Figure 13. Filtered back projection reconstruction of two uranium metal annuli. The nominal gap of 3 mm between the annuli is detectable using 1-inch imaging detectors and a 5-mm neutron production spot size.

5. CONCLUSION

The statistical model represented by Eq. (5) and the gap detection examples provide some mathematical justification for the assertion that features can be detectable despite being smaller than the neutron production spot size and detector size. The systematic errors associated with dimension quantification for the instruments that ORNL deploys require future study, such that the minimum detectable gap is currently unknown. Prior measurements have demonstrated that millimeter-scale dimensions can be accurately characterized, so the minimum gap thickness is likely also on the millimeter scale.

REFERENCE DOCUMENTS

[1] J.T. Mihalczo et al., “Physical description of nuclear materials identification system (NMIS) signatures,” NIM A 450 (2000) 531–555.

[2] J.T. Mihalczo et al., “Fast Neutron Imaging with API DT Neutron Generators,” in Proceedings of International Scientific and Technical Conference Portable Neutron Generators and Technologies on Their Basis, pp. 55–62, Moscow, Russia (2012).

[3] F. Habte, et al., "Enhancing pixelated fast-neutron block detector performance using a slotted light guide," in 2008 IEEE Nuclear Science Symposium Conference Record, pp. 3128-3132, Dresden, Germany (2008).

[4] M. A. Blackston, et al., "A Comparison of GEANT4 and DETECT2000 for the simulation of light transport in scintillation detectors," in 2008 IEEE Nuclear Science Symposium Conference Record, pp. 4995-4998, Dresden, Germany (2008).

[5] A.C. Kak and Malcolm Slaney, *Principles of Computerized Tomographic Imaging*, Society of Industrial and Applied Mathematics, 2001.

[6] K. Lange and R. Carson, “EM reconstruction Algorithms for Emission and Transmission Tomography,” *Journal of Computer Assisted Tomography* 8, 306–316 (1984).

[7] S.M. McConchie et al., *Blind Testing of NMIS Fast Neutron Imaging Measurements at INL in 2010*, Oak Ridge National Laboratory, ORNL/TM-2016/231 (2016).

[8] B.R. Grogan et al., “Alpha Detector Pixelization Effects on NMIS Imaging,” in Proceedings of the 49th Annual Meeting of the Institute for Nuclear Materials Management, 2008.

[9] J. Crye, “Enrichment Determination of Uranium Metal in Shielded Configurations Without Calibration Standards,” University of Tennessee, Knoxville Doctoral Dissertation, May 2013.